

Road Map to L_4/L_5 with a solar sail

Ariadna Farrés

**University of Maryland Baltimore County, Baltimore, Maryland, USA*

Jeannette Heiligers

†Delft University of Technology, Delft, The Netherlands

Narcís Miguel

‡Universitat Pompeu Fabra, Barcelona, Catalonia, Spain

This paper explores the capability of solar sails to transfer a probe from the displaced L_1 and L_2 libration points to the region of practical stability (RPS) around the triangular equilibrium points L_4 and L_5 . If the sailcraft arrives inside the RPS with zero synodical velocity, it will remain there with no need for station keeping maneuvers. Moreover, the location of the RPS is ideal for space weather missions as the Sun can be observed from a different angle compared to spacecraft orbiting the L_1 point. The solar sail unstable manifolds of the displaced L_1 and L_2 points come close to these regions providing opportunities for natural transfer trajectories. By varying the solar sail orientation along the manifold, the dynamics are altered and simple transfer trajectories that reach the RPS with few sail maneuvers are enabled. However, these trajectories are not optimal from a transfer time perspective, but they are used in this paper as an initial guess in a direct optimization method to find minimum-time transfers between the displaced L_1 and L_2 points and the RPS at L_4 and L_5 .

I. Introduction

Solar sails are a type of low-thrust propulsion system that take advantage of the Solar Radiation Pressure (SRP) to accelerate a small probe by means of a highly reflective surface. To date, there have been three successful solar sail demonstration missions: IKAROS by JAXA (May 2010), NanoSail-D by NASA (December 2010) and LightSail-1 by The Planetary Society (June 2016). These successes have sparked further interest in solar sailing, resulting in more scheduled demonstration missions for the upcoming two years: LightSail-2 (the follow-up of LightSail-1 by The Planetary Society) and NASA's proposed NEA Scout mission.

The unique selling point of solar sailing is the fact that its propulsive capabilities do not rely on an on-board reaction mass, which makes solar sailing the preferred option for a range of challenging mission concepts such as hovering along the Sun-Earth line sun-ward of the L_1 point (also known as the Sunjammer mission concept¹), displacing the L_1 point above the ecliptic plane for high-latitude observations of the Earth (the pole-sitter concept²), precessing an elliptical Earth-centered orbit for long residence times in the Earth's magnetotail (the GeoSail mission concept³), and even low-cost multi-rendezvous NEO missions.⁴ The purpose of the current paper is to complement this extensive list of solar sail enabled mission concepts with a preliminary study on the feasibility of solar sail transfers from the L_1 and L_2 points of the Sun-Earth Restricted Three Body Problem (RTBP) to the vicinity of the L_4 and L_5 points.

The Sun-Earth RTBP is a well-known reference model in astrodynamics and has been extensively studied in the past. It is also well known that the system exhibits five equilibrium points (L_1, \dots, L_5) whose position

*Dr., Visiting Researcher, Goddard Planetary Heliophysics Institute, University of Maryland Baltimore County, 1000 Hilltop Circle, Baltimore, Maryland 21250, AIAA Member.

†Dr., Marie Skłodowska-Curie Fellow, Delft University of Technology, Faculty of Aerospace Engineering, Kluyverweg 1, 2652 HS Delft, AIAA Member

‡Dr., Lecturer, Universitat Pompeu Fabra, Department of Information and Communication Technologies, Carrer de Tànger, 120-144 08018, Barcelona

can be artificially displaced when including a solar sail acceleration and changing its orientation.⁵ Due to their strategic location close to the Earth and their dynamical properties, periodic and quasi-periodic orbits around L_1 and L_2 have been used as reference orbits for several mission in the past such as SOHO, Genesis, GAIA, and Hershel-Plank. However, despite the fact that the orbits around L_4 and L_5 are stable and no station keeping is required, they seem to have been forgotten for mission applications as they are hard to reach. However, recent studies^{6,7} show that by adding a solar sail to accelerate the satellite, the vicinity of the L_4 and L_5 points can be reached in a reasonable amount of time.

Besides the interest from an astrodynamics perspective, the L_4 and L_5 points also hold great scientific interest as they provide a unique “side-on” view of the Sun. Such a view will be crucial in furthering the understanding of the initiation and propagation of space weather events as well as improving current space weather event forecasting capabilities. In particular, through the side-on view, the speed of coronal mass ejections (CMEs) can be measured with greater accuracy and, from L_5 , the part of the Sun’s surface that is about to rotate towards the Earth can be observed to provide a “sneak preview” of the CMEs.

This paper is part of an on-going project which intends to study the feasibility of solar sails as a propulsion system to transfer a satellite from the vicinity of the Earth to the vicinity of L_4/L_5 . One of our goals is to use the natural dynamics of the system, taking advantage of the invariant manifold structure around L_1 and L_2 ,⁸ to design transfer orbits to the practical stability region around L_4/L_5 .^{9,10} In the literature we find papers by Llanos¹¹ and Sood⁶ who study this problem from a different point of view. In both papers, they propose to depart from a parking orbit around the Earth and reach a stable periodic orbit around L_4/L_5 , a different approach than ours. Despite the differences, we intend to compare some of our results in the near future. We must note that Sood also considers solar sails as a propulsion system, while the work by Llanos considers chemical propulsion.

We propose to use the L_1 and L_2 points as gate-ways to transfer a probe to the practical stability regions around L_4/L_5 . These two regions are ideal final destination as the trajectory of a probe starting inside the region with zero velocity in synodical coordinates, will not escape for more than 1000 years. Furthermore, we will employ a two-step process to obtain time-optimal transfers. The first step consists of generating transfer orbits from the vicinity of L_1 and L_2 to a suitable neighborhood of the L_4/L_5 points by means of the unstable invariant manifolds of the former equilibria. These trajectories are sub-optimal from a transfer-time perspective due to the assumptions taken during the design process. However, they are excellent initial guesses to solve the optimal control problem of finding time-optimal transfers between L_1/L_2 and the L_4/L_5 stability regions. The second step consists of solving the optimal control problem, using the software tool PSOPT,¹² which is a particular implementation of a direct pseudo-spectral method in C⁺⁺.

In both steps, finding the initial guess and the optimization process, we consider the classical RTBP as the dynamical model, accounting for the SRP acting on the solar sail (RTBPS from now on), where the sail acceleration will depend on 3 parameters: the sail lightness number, β , (accounting for the sail efficiency), and two angles, α and δ (accounting for the sail orientation).

This paper is organized as follows, in Section II we introduce the RTBPS and describe the main parameters of the system (β , α and δ). In Section III we describe the non-linear dynamics around the two regions in the phase space that play an important role during the design process of the transfer trajectories. These are, the invariant manifold structure around the displaced L_1 and L_2 equilibrium points (subsection III.A) and the practical stability region around L_4/L_5 (subsection III.B). In Section IV we address the main goal of the paper of finding transfer trajectories between L_1/L_2 and L_4/L_5 , where subsection IV.A explains how we explore the phase space to find a piece-wise transfer trajectory and subsection IV.B takes these initial guesses to find optimal-time transfers. Some conclusions and future work are described at the end in Sections V and VI respectively.

II. Equations of Motion

We consider the Circular Restricted Three Body Problem (RTBP) including the effect of Solar Radiation Pressure (SRP) due to the solar sail (RTBPS) as a model to describe the motion of a solar sail in the Earth - Sun system. We recall that in the RTBPS we assume that the Earth and Sun are both point masses moving around their common center of mass in a circular way due to their mutual gravitational attraction. The solar sail, on the other hand, is a mass-less particle that does not affect the motion of the two primaries, but is affected by their gravitational attraction as well as by SRP.

We normalize the units of mass, distance and time, so that the total mass of the system is 1, the Earth -

Sun distance is 1 and the period of its orbit is 2π . In these units the universal gravitational constant is $G = 1$, the Earth's mass is $\mu = 3.0034806 \times 10^{-6}$, and $1 - \mu$ is the mass of the Sun. We consider a synodical reference system, where the origin is at the center of mass of the Earth - Sun system and both Earth and Sun are fixed on the x -axis (with the positive x -axis pointing towards the Earth). The z -axis is perpendicular to the ecliptic plane and the y -axis completes an orthogonal positive oriented reference system.¹³ On the left-hand side of Figure 1 a schematic representation of the main forces in the RTBPS is provided.

With these assumptions, the equations of motion in the synodical reference frame are:

$$\ddot{x} - 2\dot{y} = \frac{\partial\Omega}{\partial x} + a_x, \quad \ddot{y} + 2\dot{x} = \frac{\partial\Omega}{\partial y} + a_y, \quad \ddot{z} = \frac{\partial\Omega}{\partial z} + a_z, \quad (1)$$

where $\Omega(x, y, z) = \frac{1}{2}(x^2 + y^2) + \frac{1 - \mu}{r_{ps}} + \frac{\mu}{r_{pe}}$, $r_{ps} = \sqrt{(x + \mu)^2 + y^2 + z^2}$ and $r_{pe} = \sqrt{(x + \mu - 1)^2 + y^2 + z^2}$ are the Sun-sail and Earth-sail distances, respectively, and $\mathbf{a}_s = (a_x, a_y, a_z)$ is the acceleration due to the solar sail, where \mathbf{a}_s depends on the reflectivity properties of the sail given by the sail's lightness number (β) and the reflectivity coefficient (ρ_s); and the solar sail orientation, which is determined by the cone and clock angles (α, δ respectively).

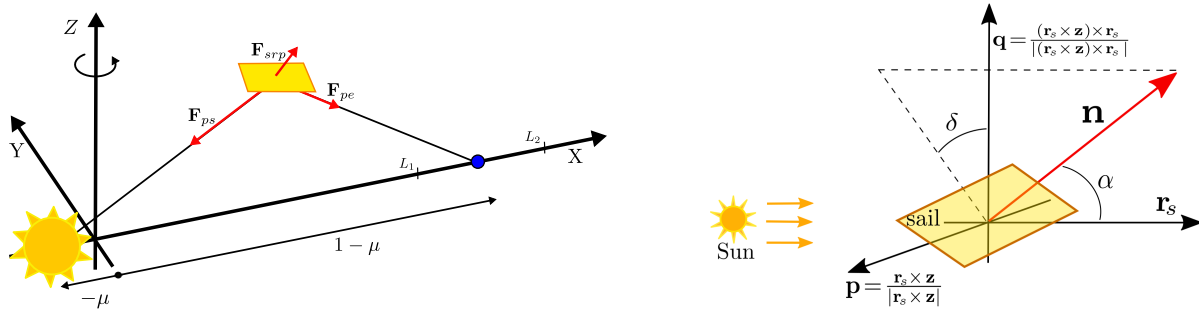


Figure 1. Left: Schematic representation of the RTBPS model. Right: Schematic representation of the reference frame used to define the sail orientation α, δ .

A. Solar Sail acceleration

The solar sail acceleration is produced by the impact of the photons emitted by the Sun on the surface of the sail, which will be reflected and absorbed by the sail material.^{5,14} For a solar sail with an area A , the force due to reflected photons is given by $\mathbf{F}_r = 2PA\langle\mathbf{r}_s, \mathbf{n}\rangle^2\mathbf{n}$ while the force due to absorption is $\mathbf{F}_a = PA\langle\mathbf{r}_s, \mathbf{n}\rangle\mathbf{r}_s$, where \mathbf{r}_s is the Sun-sail direction, \mathbf{n} is the normal direction to sail surface (both unit vectors), and $P = P_0(R_0/R)^2$ is the SRP at a distance R from the Sun (with $P_0 = 4.563 \text{ N/m}^2$ the SRP at $R_0 = 1 \text{ AU}$). If we denote ρ_a as the absorption coefficient and ρ_s as the reflectivity coefficient (which satisfy $\rho_a + \rho_s = 1$), the sail acceleration is given by:

$$\mathbf{a}_s = \frac{2PA}{m}\langle\mathbf{r}_s, \mathbf{n}\rangle \left(\rho_s\langle\mathbf{r}_s, \mathbf{n}\rangle\mathbf{n} + \frac{1}{2}(1 - \rho_s)\mathbf{r}_s \right). \quad (2)$$

We note that $\rho_s = 1$ corresponds to a perfectly reflecting solar sail, and $\rho_s = 0$ to a solar panel, where the only effect is the absorption of the photons by the panels. According to Ref. 14 a solar sail with a highly reflective aluminum-coated side has an estimated value of $\rho_s \approx 0.88$. In this paper we assume the solar sail to be flat and perfectly reflecting ($\rho_s = 1$). In future studies we plan to include the imperfections on the solar sail material and see how this affects the transfer trajectories.

1. Sail Lightness Number

We note that the SRP is proportional to the inverse square of the distance to the Sun (i.e. $P = P_0(R_0/R)^2$). It is therefore common to rewrite $2PA/m$ in Eq. 2 as a correction of the Sun's gravitational attraction:

$\beta(1-\mu)/r_{ps}^2$, where β corresponds to the sail lightness number and accounts for the sail's efficiency. Following McInnes⁵ we can see that, $\beta = \sigma^*/\sigma$, where $\sigma^* = 2P_0R_0^2/Gm_{sun} = 1.53 \text{ g/m}^2$ and $\sigma = m/A$ is the solar sail mass-to-area ratio. One can also interpret β as the ratio between the Sun's gravitational attraction and the solar sail acceleration. Another parameter used to describe the sail efficiency is through the characteristic acceleration (a_0), which represents the acceleration experienced by the sailcraft at 1 AU when the sail is perpendicular to the Sun-sail line. The characteristic acceleration and the sail lightness number are related by: $a_0 = \beta Gm_{sun}/R_0^2$.

Table 1 presents for different values of the sail lightness number (β), the corresponding mass-to-area ratio (σ), the characteristic acceleration (a_0) and the required solar sail size for 10 kg of total sailcraft mass. Near-term solar sail demonstration missions LightSail-1 and NEA-Scout have a sail lightness number of $\beta = 0.011$ and $\beta = 0.01$, respectively, while long-term mission concepts like Sunjammer require $\beta = 0.036$.

Table 1. Relation between the sail lightness number β and: the satellite's mass-to-area ratio (σ), the characteristic acceleration (a_0), and the sail area required for a satellite with 10 kg of total mass.

β	σ (g/m ²)	a_0 (mm/s ²)	Area (m ²)
0.01	153.0	0.059935	$\approx 8 \times 8$
0.02	76.5	0.119869	$\approx 12 \times 12$
0.03	51.0	0.179804	$\approx 14 \times 14$
0.04	38.25	0.239739	$\approx 16 \times 16$
0.05	30.6	0.359608	$\approx 20 \times 20$

2. Sail Orientation

The sail orientation is given by the normal direction to the surface of the sail (\mathbf{n}) and is parameterized by two angles α and δ that measure the displacement between \mathbf{n} and the Sun-sail direction $\mathbf{r}_s = (x-\mu, y, z)/r_{ps}$. Following McInnes,¹⁵ we consider the orthonormal reference frame, $\{\mathbf{r}_s, \mathbf{p}, \mathbf{q}\}$, centered at the sailcraft center of mass, with $\mathbf{p} = \frac{\mathbf{r}_s \times \mathbf{z}}{|\mathbf{r}_s \times \mathbf{z}|}$ and $\mathbf{q} = \frac{(\mathbf{r}_s \times \mathbf{z}) \times \mathbf{r}_s}{|(\mathbf{r}_s \times \mathbf{z}) \times \mathbf{r}_s|}$, and define $\mathbf{n} = \cos \alpha \mathbf{r}_s + \sin \alpha \cos \delta \mathbf{p} + \sin \alpha \sin \delta \mathbf{q}$, where α corresponds to the pitch angle (angle between \mathbf{n} and \mathbf{r}_s) and δ is the clock angle (angle between \mathbf{q} and the projection of \mathbf{n} in a plane orthogonal to \mathbf{r}_s). Figure 1 (right) shows a schematic representation of the definition of the two sail angles.

Following the definitions given above, the explicit expressions for the solar sail normal direction, $\mathbf{n} = (n_x, n_y, n_z)$, are given by:

$$\begin{aligned}
n_x &= \frac{x-\mu}{r_{ps}} \cos \alpha - \frac{(x-\mu)z}{r_2 r_{ps}} \sin \alpha \cos \delta + \frac{y}{r_2} \sin \alpha \sin \delta, \\
n_y &= \frac{y}{r_{ps}} \cos \alpha - \frac{yz}{r_2 r_{ps}} \sin \alpha \cos \delta - \frac{x-\mu}{r_2} \sin \alpha \sin \delta, \\
n_z &= \frac{z}{r_{ps}} \cos \alpha + \frac{r_2}{r_{ps}} \sin \alpha \cos \delta,
\end{aligned} \tag{3}$$

where $r_2 = \sqrt{(x-\mu)^2 + y^2}$. Notice that \mathbf{n} cannot point towards the Sun, hence $\langle \mathbf{n}, \mathbf{r}_s \rangle = \cos \alpha \geq 0$, which implies that $\alpha \in [-\pi/2, \pi/2]$ and $\delta \in [0, \pi]$.

B. Properties of the RTBPS

From a mathematical perspective the Earth-Sun-sail RTBPS is as a perturbation of the Earth - Sun RTBP, where the perturbation depends on the sail parameters ($\beta, \rho_s, \alpha, \delta$). If we consider a perfectly reflecting solar sail ($\rho_s = 1$), we can rewrite Eq. (1) as:

$$\begin{aligned}
\ddot{x} - 2\dot{y} &= \frac{\partial \tilde{\Omega}}{\partial x} + \beta \frac{1-\mu}{r_{ps}^2} \cos^2 \alpha \left(\frac{-(x-\mu)z}{r_2 r_{ps}} \sin \alpha \cos \delta + \frac{y}{r_2} \sin \alpha \sin \delta \right), \\
\ddot{y} + 2\dot{x} &= \frac{\partial \tilde{\Omega}}{\partial y} + \beta \frac{1-\mu}{r_{ps}^2} \cos^2 \alpha \left(\frac{-yz}{r_2 r_{ps}} \sin \alpha \cos \delta - \frac{x-\mu}{r_2} \sin \alpha \sin \delta \right), \\
\ddot{z} &= \frac{\partial \tilde{\Omega}}{\partial z} + \beta \frac{1-\mu}{r_{ps}^2} \cos^2 \alpha \left(\frac{r_2}{r_{ps}} \sin \alpha \cos \delta \right),
\end{aligned} \tag{4}$$

where $\tilde{\Omega}(x, y, z) = \frac{1}{2}(x^2 + y^2) + (1 - \beta \cos^3 \alpha) \frac{1 - \mu}{r_{ps}} + \frac{\mu}{r_{pe}}$.

It is well known that the classical RTBP (no solar sail) is Hamiltonian, but when we include the perturbation due to the solar sail, the Hamiltonian structure of the system breaks down. The system is Hamiltonian only for $\alpha = 0$ (i.e., the solar sail is oriented perpendicular to the Sun-sail line) and $\alpha = \pm\pi/2$ (i.e., no sail effect). The system is time reversible for $\alpha \neq 0, \delta = 0$ (i.e., the orientation of the solar sail varies vertically with respect to the Sun-sail line).¹⁶ In these two particular cases, for a fixed sail orientation, we can ensure the existence of families of periodic and quasi-periodic orbits around an equilibrium point.^{17, 18}

As in the RTBP, we define the Jacobi function as:

$$J_c = \dot{x}^2 + \dot{y}^2 + \dot{z}^2 - 2\tilde{\Omega}(x, y, z), \quad (5)$$

where for $\beta = 0$ (i.e., no sail) and for $\beta \neq 0, \alpha = 0$ (a sail perpendicular to the Sun-sail line), this function corresponds to the Jacobi constant of the RTBP or RTBPS (Hamiltonian case). If $\alpha \neq 0$ this function is not constant but it can still be used to classify types of motion.^{16, 19}

We note that the system also satisfies the following symmetries:

$$\begin{aligned} S1 : (t, x, y, z, \alpha, \delta) &\mapsto (-t, x, -y, -z, -\alpha, \delta), \\ S2 : (t, x, y, z, \alpha, \delta) &\mapsto (-t, x, -y, z, \alpha, -\delta), \end{aligned} \quad (6)$$

which we can take advantage of when we compute equilibrium points and periodic orbits or when we describe the dynamics of the system.

1. Equilibrium Points

It is well known that when we discard SRP ($\beta = 0$) the Earth-Sun RTBP has five equilibrium points,¹³ and that all of them lie in the ecliptic plane ($z = 0$). Three of them, known as the *collinear points* $L_{1,2,3}$, are on the line joining the two primaries ($y = 0$). The other two, known as the *triangular points* $L_{4,5}$, lie in the ecliptic plane, and form an equilateral triangle with the two primaries (i.e., their distance to both Earth and Sun is 1). The three collinear points are all linearly unstable (saddle×center×center), whereas the two triangular points are linearly stable (center×center×center).

If the sail is oriented perpendicular to the Sun-sail line ($\alpha = 0$) the system presents a similar phase space portrait as for $\beta = 0$. We also have five equilibrium points $SL_{1,\dots,5}$ in the ecliptic plane, siblings to the classical $L_{1,\dots,5}$ but displaced towards the Sun.¹⁵ The three collinear points ($SL_{1,2,3}$) still lie on the Earth-Sun line, and are linearly unstable (saddle×center×center), while the two triangular points ($SL_{4,5}$) no longer form an equilateral triangle: their distance to the Earth is 1, but the distance to the Sun behaves as $(1 - \beta)^{1/3}$. $SL_{4,5}$ are also linearly stable for all β .

We recall that there is no explicit expression for the three collinear equilibrium points, but that their position can be found by solving a quintic. We can define, $\gamma_{1,2}$ as the distance from $SL_{1,2}$ to the Earth, and γ_3 as the distance from SL_3 to the Sun. It can be seen that γ_i is the only positive solution to the quintic equation:^{13, 15}

$$\gamma_1^5 + (3 - \mu)\gamma_1^4 + (3 - 2\mu)\gamma_1^3 - (\mu\beta - \beta + \mu)\gamma_1^2 - 2\mu\gamma_1 - \mu = 0, \quad (7)$$

$$\gamma_2^5 - (3 - \mu)\gamma_2^4 + (3 - 2\mu)\gamma_2^3 + (\mu\beta - \beta - \mu)\gamma_2^2 + 2\mu\gamma_2 - \mu = 0, \quad (8)$$

$$\gamma_3^5 + (2 + \mu)\gamma_3^4 + (1 + 2\mu)\gamma_3^3 - (1 - \mu)(1 - \beta)\gamma_3^2 - 2(1 - \mu)(1 - \beta)\gamma_3 - (1 - \mu)(1 - \beta) = 0, \quad (9)$$

and $SL_1 = (1 - \mu - \gamma_1, 0, 0)$, $SL_2 = (1 - \mu + \gamma_2, 0, 0)$ and $SL_3 = (-\mu - \gamma_3, 0, 0)$. On the other hand, there is an explicit expression for the triangular points for all β :

$$SL_{4,5} = (x_{4,5}, y_{4,5}, 0) := \left(-\mu + \frac{(1 - \beta)^{2/3}}{2}, \pm(1 - \beta)^{1/3} \left[1 - \frac{(1 - \beta)^{2/3}}{4} \right]^{1/2}, 0 \right). \quad (10)$$

Finally, if we change the sail orientation ($\alpha \neq 0$ or/and $\delta \neq 0$) we artificially displace the position of the equilibrium points. For instance, if we take $\delta = \pm\pi/2$ and vary α , we displace the equilibrium points to one side or the other of the Sun-sail line inside the ecliptic plane; while if we take $\delta = 0, \pi$ and vary α we displace the equilibrium points above or below the ecliptic plane, where all the displaced equilibria lie in a plane perpendicular to $z = 0$ containing L_i and SL_i . When we take any other fixed value of $\delta = \delta^*$ and vary α , we displace the equilibrium points on an inclined plane with respect to the ecliptic containing L_i and SL_i .^{16, 20, 21}

III. Non-Linear dynamics around equilibria

We recall that the main goal of this paper is to find feasible transfer orbits to the L_4 and L_5 vicinity. For this purpose we propose to use the unstable invariant manifolds around the displaced SL_1 and SL_2 equilibrium points. It is true that the unstable invariant manifold structure around the libration point is more complex and one should also consider the different families of periodic and quasi-periodic orbits. But including the solar sail parameters already broadens the range of possibilities and for this preliminary work we only focus on them. As for the vicinity of L_4 and L_5 , it is well known that there is a large practical stability region where trajectories starting there will remain in the region for more than 1000 years with no need of station keeping maneuvers, which makes this location ideal for a space-weather observatory.

In this section we will analyze the non-linear dynamics around the different equilibrium points and how these are affected by the different sail parameters: β , α and δ .

A. SL_1 and SL_2 equilibrium point

Let us focus on the dynamics close to the displaced collinear points SL_1 and SL_2 , which we recall are equilibrium points for $\beta \neq 0$ and $\alpha = 0$ (solar sail oriented perpendicular to the Sun-sail line). We already mentioned that as β increases these equilibrium points are shifted towards the Sun, and that the linear dynamics for SL_1 and SL_2 are always center \times center \times saddle. Table 2 summarizes the position and the eigenvalues of SL_1/SL_2 for $\beta = 0.01, \dots, 0.05$. As the system is Hamiltonian for $\alpha = 0$, the two center directions give rise to two families of periodic orbits, the well-known planar and vertical Lyapunov orbits. Moreover, the coupling between the two oscillatory motions gives rise to the Lissajous and Halo family of orbits. All these orbits are also known as Libration Point orbits (LPOs).

Nevertheless, in this paper we want to focus on the dynamics given by the saddle component, as it gives rise to the stable and unstable manifolds which together with the stable and unstable manifold of the LPOs configure the set of reentry and escape trajectories related to the equilibrium points vicinity. Notice that as β increases the instability rate of SL_1 decreases while the instability rate of SL_2 increases, which has a direct effect on the rates of escape from the vicinity of the equilibrium point.

Table 2. For different values of β , position of the displaced equilibrium points SL_1 and SL_2 , and values of the three pair of eigenvalues $\pm\lambda$, $\pm i\omega_1$ and $\pm i\omega_2$.

β	SL_1	λ	ω_1	ω_2	SL_2	λ	ω_1	ω_2
0.01	0.98873101897	2.13994	1.8517	1.7749	1.00908250142	2.88718	2.3061	2.2399
0.02	0.98716671573	1.78196	1.6484	1.5679	1.00827979413	3.30472	2.5719	2.5113
0.03	0.98525423949	1.46959	1.4821	1.4010	1.00762463476	3.72982	2.8482	2.7927
0.04	0.98299017728	1.20876	1.3536	1.2762	1.00708319765	4.15761	3.1307	3.0797
0.05	0.98040996743	9.98326	1.2586	1.1886	1.00662972805	4.58492	3.4162	3.3691

The unstable manifolds of the displaced SL_1 and SL_2 equilibria are the perfect candidates to provide trajectories to reach the L_4/L_5 neighborhood. To illustrate this we have computed the stable and unstable manifolds related to SL_1 and SL_2 for different values of β . This will give us an idea of the general trend of the invariant manifolds, and how the efficiency of the solar sail affects them. Figure 2 shows the stable and unstable manifolds for $\beta = 0$ (left), 0.01 (middle) and 0.03 (right). A general view and their relative position with respect to a subset of the practical stability region appears in the top plots. The bottom plots show a zoomed-in image close to the Earth. We note that all these invariant manifolds have been computed up to $t_f = 10$ years. Hence, the longer the unstable manifold path is, the faster the transfer to L_4/L_5 can be. These results are consistent with the values presented in Table 2.

It is interesting to note that, for $\beta = 0$ (i.e., no sail), we can only reach L_4 from L_2 and L_5 from L_1 . But the extra effect due to the solar sail ($\beta \neq 0$) allows us to reach L_4 and L_5 from L_1 . This is very convenient for the mission scenario where we consider two satellites, one aiming for L_4 and the other for L_5 , as we could use the same launch vehicle to reach the L_1 invariant manifolds. On the other hand, from L_2 for all values of β we can only reach L_5 as the unstable invariant manifolds get trapped around the Earth.

As solar sails are orientable surfaces, we have checked how an initial change in the sail orientation can affect the trajectory of an initial condition starting along the unstable manifolds that we have just shown. We recall that, when we change the sail orientation we displace the equilibrium point as well as the saddle

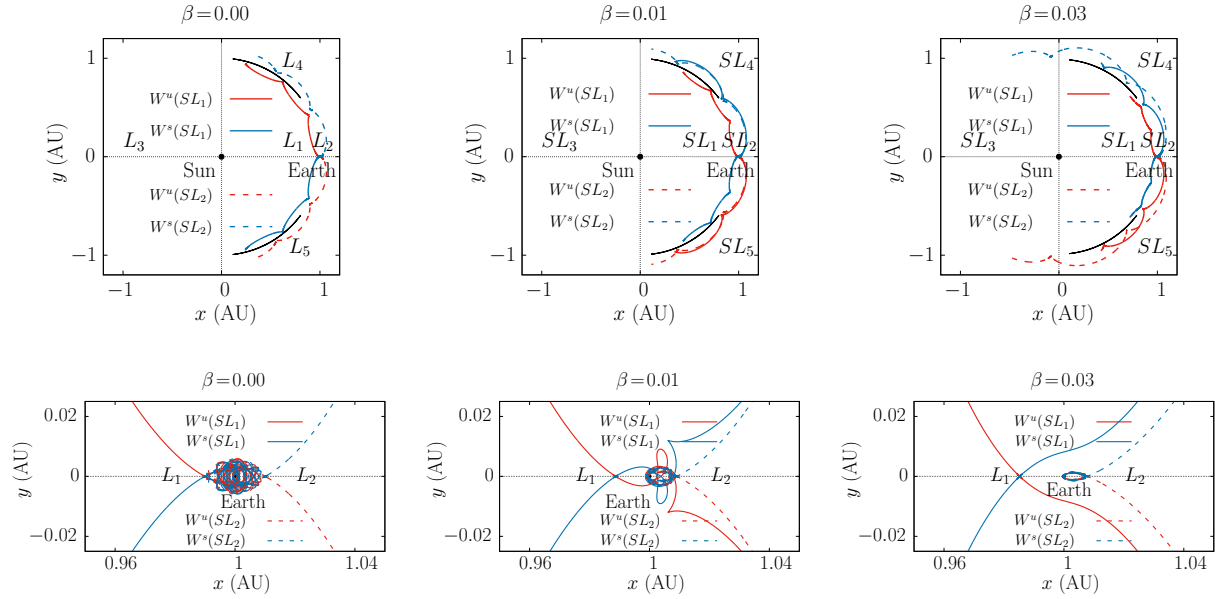


Figure 2. Stable (blue) and Unstable (red) manifolds of SL_1 and SL_2 for $\beta = 0, 0.01$ and 0.02 and $\alpha = 0$. Top: general view and relation with the practical stability (black). Bottom: zoom of these manifolds close to the Earth.

position.^{7,22} Hence, the trajectories will escape along the new unstable direction. This can have interesting implications on the trajectories of initial conditions close to SL_1 and SL_2 unstable manifolds. In Figure 3 we show the trajectories for different values of α of the same two initial condition \mathbf{p}_0 along the unstable direction of the SL_1 equilibrium point (i.e. $\mathbf{p}_0 = SL_1 \pm h\mathbf{v}^u_1$ and $h = 10^{-4}$). As we can see, for each of the sail orientations the final trajectories are completely different. For instance, for $\alpha = 20^\circ$ (middle) the behavior is quite similar to the one for $\alpha = 0$ (Figure 2 middle) where each leg of the the unstable manifolds leads to different regions of the phase space, in particular L_4 and L_5 . On the other hand, for $\alpha = 15^\circ$ (left) the two legs of the unstable manifolds come close to the Earth and then move towards L_5 , and for $\alpha = -25^\circ$ (right) the two legs of the unstable manifolds are directed towards L_4 . This shows us how rich the dynamics around the equilibrium points can be when changing the sail orientation.

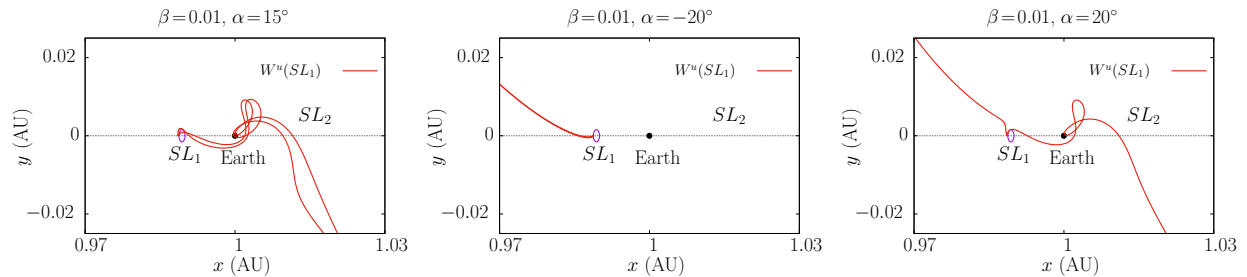


Figure 3. For $\beta = 0.01$, propagation of an initial condition on the SL_1 unstable manifold for $\alpha = 15^\circ$ (left), $\alpha = 25^\circ$ (middle) and $\alpha = -25^\circ$. We only show the vicinity of the Earth and the two collinear points.

Figure 4 shows the same analysis for initial conditions \mathbf{p}_0 along the SL_2 unstable manifold (i.e. $\mathbf{p}_0 = SL_2 \pm h\mathbf{v}^u_2$ and $h = 10^{-4}$). Here we notice that for different values of α , the trajectories can either go towards the Earth, or lead towards L_5 . As SL_2 gets closer to the Earth as β increases, it is harder to find escape trajectories towards L_4 as one of the legs gets entangled in the Earth's vicinity, where the dynamics are very chaotic. This does not mean that there are no transfers from SL_2 to L_4 , this only implies that there is a small set of sail orientations that enables such paths.

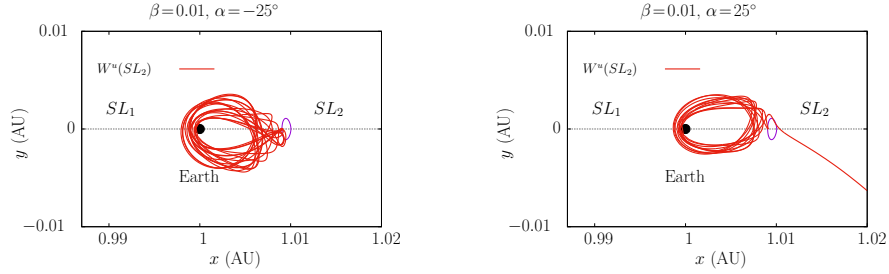


Figure 4. For $\beta = 0.01$, propagation of an initial condition on the SL_2 unstable manifold for $\alpha = 25^\circ$ (left) and $\alpha = -25^\circ$. We only show the vicinity of the Earth and the two collinear points.

B. Determination of a target region

Recall that for the Earth-Sun RTBPS, the triangular Lagrangian points SL_4/SL_5 are totally elliptic equilibria. Under generic conditions, the KAM theorem applies around these kind of points and most of the initial conditions in a small enough neighborhood of SL_4/SL_5 lie on 3D invariant tori. That is, a region of stability, understood in a practical sense, is expected to be found close enough to SL_4/SL_5 .

Here we are going to study the regions of practical stability (RPS from now on) around SL_4/SL_5 for $\beta = 0.01, 0.02, \dots, 0.05$. An initial condition (initial position of the probe) close to SL_4/SL_5 with zero synodical velocity $\dot{x} = \dot{y} = \dot{z} = 0$ is regarded as *practically stable* if the corresponding trajectory remains close to SL_4/SL_5 for a large time span. The RPS is the set of practically stable points, and can be mathematically defined as the subset of a box R (in appropriate coordinates) that contains SL_4/SL_5 such that if we propagate the orbit starting at R with $\dot{x} = \dot{y} = \dot{z} = 0$, it does not leave a larger set R' after a large number of years $T \gg 0$. In Figure 5 we show the choice of R and R' for the problem we are dealing with. Here the boundary of R' defines the *escaping criterion*: if an orbit crosses this boundary we consider that it does not belong to the RPS. Note that, since we are assuming that the trajectories start with zero synodical velocity, the RPS is a 3D set. But for the purposes of this contribution, we restrict ourselves to the section of the RPS to the ecliptic plane $z = 0$.

Despite the available theory of Hamiltonian dynamical systems gives very valuable information about the evolution of the system around SL_4/SL_5 , it fails when it comes to describe the shape of the full region where invariant tori lie. Furthermore, the description of the invariant objects that conform the boundary of this region is still an open and hard mathematical problem.¹⁰ Even with the techniques available nowadays, only brute-force explorations have been useful to give the most basic descriptions.

To study the RPS in concrete problems, one relies on simulation and for that, one has to fix a maximal number of years T . Of course, the shape and size of the detected RPS depends strongly on T . Since we will deal systematically with numerical approximations with some fixed resolution, one expects to be able to find, for each choice of the values of the parameters of the system, a value of $T = T_{\max}$ such that the differences with the detected RPS for T_{\max} and for any $T > T_{\max}$ are negligible. For the sets of parameters we have studied here we had to reach $T_{\max} = 10^4$ years. Recall that a generic orbit close to a totally elliptic equilibrium point of a Hamiltonian system with three or more degrees of freedom will eventually escape due to the so-called Arnold diffusion, but it would take exponentially long times. This concerns the mathematical problem within, but for mission applications, a study for $T = 10^3$ years is more than enough.

1. Approximation of the RPS

Due to the symmetries of the system, it is sufficient to study the RPS around one of the two triangular equilibria, so in the following we are going to restrict ourselves to the dynamics around SL_4 .

The most efficient way to approximate the RPS in sections $z = 0$ is using a brute-force exploration of a region close to SL_4 for some value of $T = T_0$, and perform a sequence of refinements for larger values of $T > T_0$ by only checking again the boundary of the first approximation. Due to the shape of this region in x, y coordinates, see Figure 6 left, it is convenient to change to polar coordinates $(r, \theta) \in (-(1 - \beta)^{1/3}, \infty) \times [-0.5, 0.5]$ (measured in AU and $\text{rad}/(2\pi)$, respectively) whose origin of coordinates corresponds to the

position of SL_4 :

$$x = \mu + (r + r_4) \cos(2\pi\theta + \theta_4), \quad y = (r + r_4) \sin(2\pi\theta + \theta_4), \quad (11)$$

where $r_4 = \sqrt{(x_4 + \mu)^2 + y_4^2}$, $\theta_4 = \arctan(y_4/(x_4 + \mu))$ are the polar coordinates of SL_4 , see Eq. 10. Note that positive angles are counted counterclockwise. So, the points in the RPS closest to the Earth correspond to the smallest (negative) values of θ .

Now we describe briefly the method we used to approximate the RPS. We refer to Ref. 10, 23 for a more detailed exposition. For each value of $z = 0$ we proceed as follows:

Step 1: First approximation. Fix $T = T_0$ and an equispaced grid of points in some adequate box R in (r, θ) . Each point in the grid defines an initial condition $(x(r, \theta), y(r, \theta), 0, 0, 0, 0)$ according to Eq. 11, and these are integrated for $T = T_0$ years. The *escaping criterion* here is to cross the hypersurface $y = -0.5^{24}$ (see Figure 5). So, if for some $t < 2\pi T_0$ it happens that $y < -0.5$, we will consider that the initial condition does not belong to the RPS. If we manage to integrate until $t = 2\pi T_0$ without this happening, we consider that the initial condition belongs to the RPS.

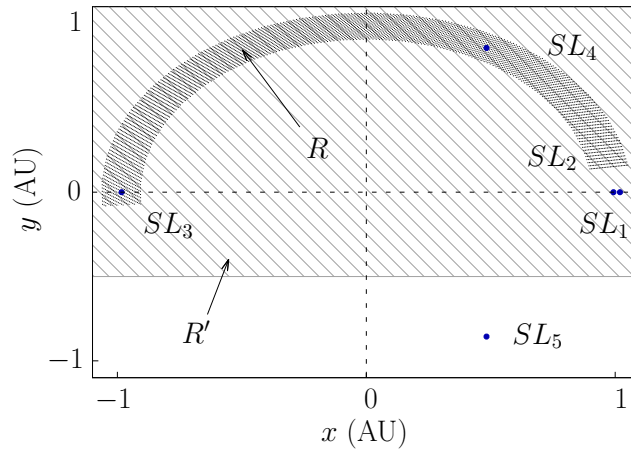


Figure 5. Schematic view of the phase space. The Sun and the Earth are close to the origin of coordinates and are not distinguishable at the displayed scale. Here we depict the typical region where initial conditions are chosen ($R = [-0.08, 0.08] \times [-0.15, 0.35]$) and the region in which they have to remain for T years for them to be considered as stable in a practical sense (R'). The escaping criterion is to cross the boundary of R' : $y = -0.5$.

Step 2: Successive refinements. The first refinement consists in considering $T_1 > T_0$, and in integrating again the points in the grid that are boundary points. Boundary points are points that belong to the RPS for $T = T_0$ such that at least one of its adjacent neighbors escaped. These points are classified according to the same escaping criterion but now with T_1 instead of T_0 : if for some $t < 2\pi T_1$ it happens that $y < -0.5$, it is an escaping point and non-escaping otherwise. Note that every time a boundary point escapes for T_1 , it changes the shape of the boundary and generates more boundary points, so this process has to be repeated until none of the points on the boundary escapes in at least T_1 years.

This process can be repeated for a sequence of increasing values of T , $T_2 < T_3 < \dots < T_n$ until we reach the desired T_{\max} .

This method reduces substantially the computational cost to determine the RPS, since it avoids reiterating points closer to SL_4 , where one expects exponentially long trapping times, and only the fastest escaping initial conditions are studied.

Here we are interested in transfers to SL_4/SL_5 in the ecliptic plane. Hence, in what follows, unless stated otherwise, we will refer to the section of the RPS in $\{z = 0\}$ simply as RPS.

2. A common target region for $\beta \leq 0.05$

For realistic values of β , one does not expect the shape and size of the RPS to differ much from the non-sail case $\beta = 0$. We started by studying the evolution of the RPS as β increases from 0.

To do so, we have considered a 1000×1000 grid in $(r, \theta) \in R = [-0.0008, 0.0008] \times [-0.35, 0.15]$, and $\beta = 0.01, \dots, 0.05$, see Figure 5 for a depiction of a similar region, but 100 times wider. It is worth noting that for all these cases we had to consider $T_{\max} = 10^4$ years^a. For smaller values of T the region appears to be much larger and to have a less defined boundary. In Figure 6 we show the region for $\beta = 0.01$ and for $\beta = 0.05$. The left panel depicts the approximation of the region in actual x, y coordinates, while the right panel shows a detailed view of these two examples in (r, θ) coordinates. The fact that these are centered in SL_4 allows for comparison.

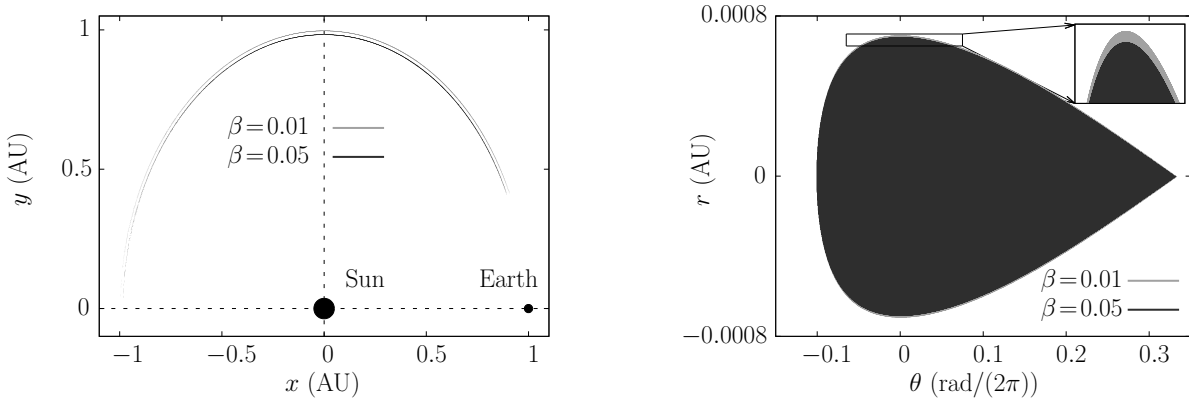


Figure 6. Section in $z = 0$ of the RPS around L_4 for $\beta = 0.01$ and $\beta = 0.05$. **Left:** Original coordinates x, y . **Right:** Detail in (r, θ) coordinates.

A global picture of the obtained results can be described as follows: in all the studied cases, we observe that the RPS is extremely narrow in r compared with θ . More concretely, the regions have, approximately, a width of 0.0016 AU and a length of π AU. This is a difference of 3 orders of magnitude. Also, the region moves towards the position of the Sun as β increases, as does the SL_4 point, see Eq. 10. Moreover, for the studied values of β , the area of the RPS seems to decrease close to linearly as β increases. This behavior is lost once one considers larger values of β ,²³ see the detail in the right plot in Figure 6. We provide, for the values of β that are of our interest, the corresponding area of the RPS in Table 3.

Table 3. Relation between the sail lightness number β and the area of the RPS computed up to $T = 10^4$ years

β	Area (AU ²)	Area (km ²)
0.01	0.000400	8.97×10^{12}
0.02	0.000399	8.93×10^{12}
0.03	0.000398	8.90×10^{12}
0.04	0.000396	8.87×10^{12}
0.05	0.000395	8.83×10^{12}

Despite these minor differences, it seems that, after translating SL_4 to the origin, it makes sense to define a region in (r, θ) coordinates that can serve as target for prospective missions, as we will study later on in this contribution.

According to KAM and Nekhorosev theories, the RPS around SL_4/SL_5 are due to the presence of nested 3D invariant tori that collapse at these two equilibria. If we consider an orbit on one of these 3D tori or very close to it, its trajectory would be seen as oscillating in the x, y projection. Of course, the amplitude of these oscillations will tend to 0 as the chosen torus is closer to SL_4/SL_5 . For mission applications, it therefore makes sense to choose a target region according to the amplitude of these oscillations.

^aThe computation for each value of β takes approximately 20h of CPU time.

We measure these oscillatory motions by keeping track of how much the coordinates (r, θ) vary along the trajectories starting from initial conditions chosen in the RPS. So, during the course of the integration, we compute the maximal and minimal values of r and θ attained during the the orbit and denote them as r_M , r_m , θ_M and θ_m . Then, the observables to take into account are

$$\Delta r = r_M - r_m, \quad \Delta \theta = \theta_M - \theta_m.$$

For all studied values of $\beta \in [0, 0.05]$, and all initial conditions that belong to the RPS, we observed that $\Delta r \in [0, 0.01]$ AU and $\Delta \theta \in [0, 0.45]$ rad/ (2π) computed among all the initial conditions that belong to the RPS. Of course the initial conditions that led to smaller Δr and $\Delta \theta$ are those closer to $r = 0$ and $\theta = 0$, that is, closer to SL_4 . The outermost points of the RPS are those that experiment wider oscillations: in the course of propagation of the initial conditions in the RPS, the r coordinate can move over 10^7 km and in the θ coordinate, these points can range most of the first two quadrants in the x, y plane.

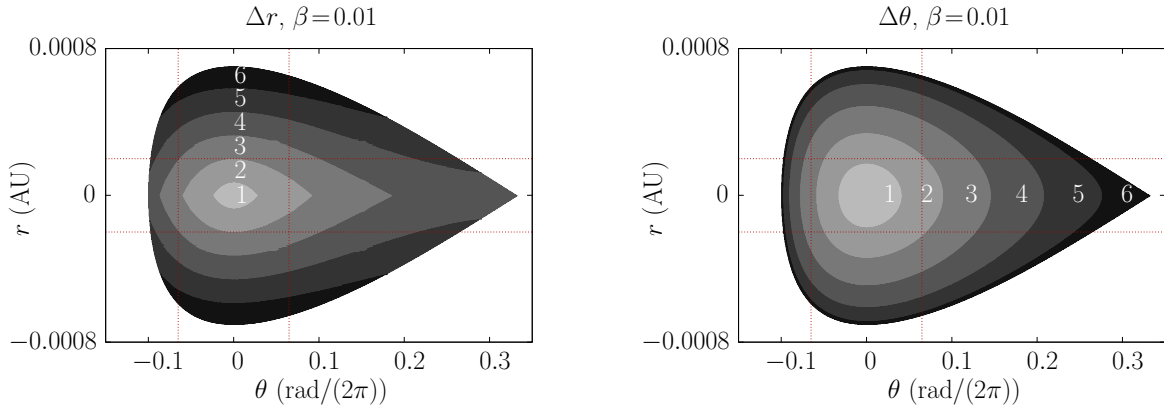


Figure 7. Oscillations of orbits starting at the RPS for $\beta = 0.01$, computed with $T = 10^3$ years. Left: Δr . Right: $\Delta \theta$. Each shade of gray indicates a certain interval of the oscillations: the subsets labeled with $i = 1, \dots, 6$ correspond to initial conditions for which $\Delta r \in [(i-1) \cdot 0.0017, i \cdot 0.0017]$ and $\Delta \theta \in [(i-1) \cdot 0.075, i \cdot 0.075]$. The vertical (resp. horizontal) red dotted lines correspond to $\theta = \pm 0.065$ (resp. $r = \pm 0.0002$).

We represent the increase of the amplitude of the oscillations in Figure 7. There each of the 6 regions correspond to initial conditions whose corresponding orbits oscillate in Δr and $\Delta \theta$ in some interval. These intervals were chosen so that they had the same length.

For mission applications, one is led to consider target positions of the probe that oscillate in a controlled manner. So, for the optimization problem in the forthcoming sections we are going to choose, as target points, a region in the left and right panels of Figure 7 that is close to SL_4 : approximately the region labeled with a 2. Up to $T = 1000$ years, these orbits experiment oscillations of at most $\Delta r < 0.034$ AU and $\Delta \theta < 0.15$ rad/ (2π) . It appears that a good approximation of this region is the interior of the ellipse

$$\mathcal{R} : \left(\frac{r}{r_{\max}} \right)^2 + \left(\frac{\theta}{\theta_{\max}} \right)^2 \leq 1, \quad (12)$$

where $r_{\max} = 0.0002$ and $\theta_{\max} = 0.065$. Despite being a relatively large set of target orbits, we will study the optimization problem for a smaller set by reducing the value of θ_{\max} at the end of Sect. IV.B.

To illustrate how the orbits inside the RPS behave, we propagated two orbits within region \mathcal{R} for $\beta = 0.01$: one starting at $(r_0, \theta_0) = (0, 0.0325)$ and another one starting at $(r_0, \theta_0) = (0.0001, 0)$. These correspond, respectively, to the left and right panels of Figure 8. To be able to see oscillations, we had to integrate up to $T = 500$ years. Since the width of the region in the x, y coordinates is very narrow, it is convenient to use again the (r, θ) coordinates to visualize the motion of the probe.

In both panels of Figure 8 we observe that there is some regularity in the motion. It is plausible to think that these orbits are close to a 3D KAM invariant torus. Qualitatively, these orbits display distinctive features. On the left, we observe that the projection of orbits starting at $r = 0$ in the (r, θ) plane oscillate both in r and θ always with the same amplitude, while for $r \neq 0$, where the amplitude of the oscillations in

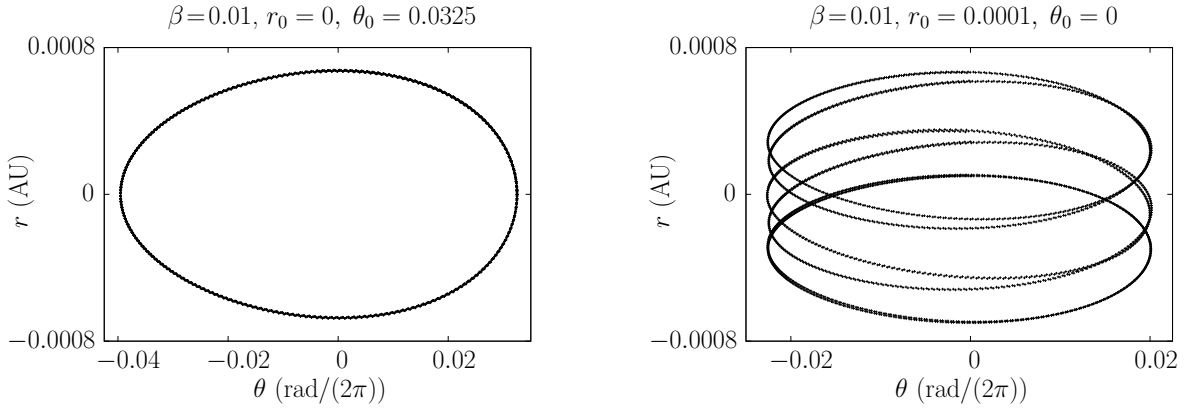


Figure 8. Examples of orbits inside the RPS for $\beta = 0.01$. **Left:** $(r_0, \theta_0) = (0, 0.0325)$. **Right:** $(r_0, \theta_0) = (0.0001, 0)$.

r changes much more along the propagation. This depends on which 3D KAM torus the orbit evolves close to. This problem requires further investigations and is left for future contributions.

IV. Transfer to L4 and L5

As we have already mentioned, we propose to use the L_1 and L_2 points as gate-ways to transfers towards the subset \mathcal{R} in the RPS at L_4/L_5 . We employ a two-step process to obtain time-optimal transfers. First we generate transfer orbits taking advantage of the unstable manifolds related to the displaced L_1 and L_2 . These candidates trajectories are constructed as a concatenation of piece-wise arcs, where the sail orientation is kept constant throughout each of the arcs. These solutions are then used as an initial guess to find time-optimal transfer trajectories between the displaced L_1/L_2 points and a subset of the L_4/L_5 practical stability regions.

A. Finding an Initial Guess

We propose a simple transfer strategy to reach $\mathcal{R} \subset \text{RPS}$ at $SL_{4,5}$ which only requires three maneuvers: (1) set $\alpha = \alpha_0$ and travel along the unstable manifold related to an equilibrium point p_0 from the SL_1/SL_2 families; (2) when we reach a given Poincaré section Σ_1 , we change the sail orientation to $\alpha = \alpha_1$ and insert the sail on a transfer trajectory that reaches \mathcal{R} in the RPS around $SL_{4,5}$; and (3) once we reach \mathcal{R} we set the sail perpendicular to the Sun-sail line ($\alpha = 0^\circ$) to remain there. For the Poincaré section we use $\Sigma_1 = \{y = \pm(x - \mu)/\sqrt{3}\}$, a hyper-plane at the mid-distance between the Earth-Sun line and the $SL_{4,5}$ -Sun line. Note that this particular hyper-plane cuts through the xy plane $\pm 30^\circ$ from the xz plane; other Poincaré sections could be considered but this one is chosen as the hyper-plane is at the same distance from $L_{1,2}$ as from $L_{4,5}$. In Figure 9 we have a schematic representation of this three step strategy.

To generate these transfer trajectories, we have performed a brute-force search. For a fixed β , we have taken different initial conditions (\mathbf{x}_0) along the two direction of the unstable vector ($\mathbf{v}_{1,2}^u$) related to SL_1 and SL_2 respectively (i.e. $\mathbf{x}_0 = SL_{1,2} \pm h\mathbf{v}_{1,2}^u$ and $h = 10^{-5}, 5 \times 10^{-5}, 10^{-4}$). For each initial condition (\mathbf{x}_0) we have considered a set of different fixed sail pitch angles $\alpha_i \in [-65^\circ, 65^\circ]$, and integrated (forward in time) until the trajectory reaches Σ_1 . Additionally, we take a grid of initial conditions in the subset \mathcal{R} of the $SL_{4,5}$ RPS (i.e. $x = (r + r_{4,5}) \cos(2\pi\theta + \theta_{4,5}) - \mu$, $y = (r + r_{4,5}) \sin(2\pi\theta + \theta_{4,5})$, $z = \dot{x} = \dot{y} = \dot{z} = 0$ where (r, θ) satisfy $(\frac{r}{r_{max}})^2 + (\frac{\theta}{\theta_{max}})^2 \leq 1$ and $r_{max} = 0.0002$ and $\theta_{max} = 0.065$). Again for each point in the region we integrate the trajectory (backwards in time) with different fixed sail orientations ($\alpha_j \in [-65^\circ, 65^\circ]$) until the trajectory reaches Σ_1 . In both cases if the trajectory comes too close to the Earth ($r_{pe} < 10^{-4}$ AU) or takes more than 10 years to reach Σ_1 we stop the integration and discard the trajectory. Finally, we compare the two sets of points, the ones arriving from $SL_{1,2}$ with those arriving from $SL_{4,5}$, on the section Σ_1 to determine intersections (or quasi-intersections) in position and velocity. We will perform a first filtering process where we discard all trajectories where the difference in position at Σ_1 is larger than 5×10^{-4} AU and where the

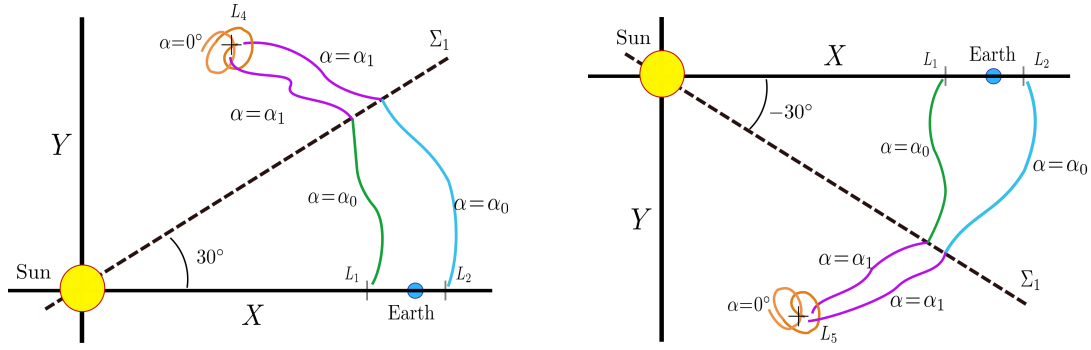


Figure 9. Schematic representation of a 3 stage transfer strategy from the SL_1, SL_2 vicinity to a subset of the SL_4 and SL_5 practical stability regions.

required sail orientation change ($\Delta\alpha$) at Σ_1 is larger than 60° . All the resulting trajectories, although they have a discontinuity at the section, are candidate trajectories to be refined with a shooting method or can be used as an initial guess for the optimization problem.

We have performed the brute-force search process described above for $\beta = 0.01$, and the transfer trajectories from: (a) SL_1 to SL_4 , (b) SL_1 to SL_5 , (c) SL_2 to SL_4 and (d) SL_2 to SL_5 . Table 4 summarizes for each of the 4 cases the transfers we have analyzed the transfer time t_f to reach \mathcal{R} , the required change in the sail orientation $\Delta\alpha$ at Σ_1 and the difference in velocity Δv at Σ_1 . We recall that, despite that these trajectories have been filtered, all these trajectories have a discontinuity in position and velocities at Σ_1 and a shooting method should be performed by varying the initial conditions at SL_1/SL_2 and at $\mathcal{R} \subset \text{RPS}$ to eliminate this discontinuity. Notice that there is a larger set of possible transfer orbits from SL_1 to both the SL_4 and SL_5 than starting around SL_2 . There is also a larger range of different transfer times and Δv at the section.

Table 4. For the filtered

	# filtered	$\Delta\alpha$ (min-max)	estimated transfer times	estimated Δv at Σ_1
SL_1 to SL_4	15774	$20^\circ - 60^\circ$	ranges from 681 to 1530 days	from 270 to 600 m/s
SL_1 to SL_5	1557	$20^\circ - 55^\circ$	ranges from 1250 to 4000 days	from 500 to 150 m/s
SL_2 to SL_4	93	$20^\circ - 45^\circ$	≈ 3568 days	≈ 500 m/s
SL_2 to SL_5	1414	$35^\circ - 50^\circ$	≈ 988 days	≈ 600 m/s

From all these trajectories we have selected, from each of the $SL_{1,2}$ to $SL_{4,5}$ sequences, two candidate trajectories can be used as initial guesses for solving the time-optimal problem: the one with the minimum transfer time and the one with the minimum Δv at the section. Figure 10 shows the candidate transfer trajectories with minimum time from the SL_1 unstable manifold to SL_4 (green) and SL_5 (purple). If we look at the behavior of these trajectories close to the Earth (Figure 10 right) we notice how the trajectory performs a fly-by close to the Earth to reach the vicinity of SL_2 before it starts the excursion towards SL_5 . This would explain the difference in transfer times that we see in Table 4 where the transfer trajectories from SL_1 to SL_4 take between 681 to 1530 days and the transfers from SL_1 to SL_5 take between 1298 to 4000 days. Figure 11 shows the minimum time candidate transfer trajectory starting from the SL_2 unstable manifold to SL_4 (green) and SL_5 (purple). Notice that here the transfer trajectory toward SL_4 performs a long excursion passing close to SL_5 . This is due to how we have constructed the trajectories and due to the fact that the first leg from the unstable manifolds around SL_2 either goes towards the Earth or leaves towards SL_5 . This large excursion causes the transfer times that we have in Table 4 where the transfer to SL_4 takes more than 3 times the transfer time to SL_5 .

B. Optimized Solutions

While the results of Section IV.A provide valuable insights in the capability of solar sails to transfer between the displaced L_1 and L_2 points and the region \mathcal{R} at L_4/L_5 , the obtained trajectories are sub-optimal from a transfer time perspective due to the assumption of the piece-wise constant attitude of the solar sail. In

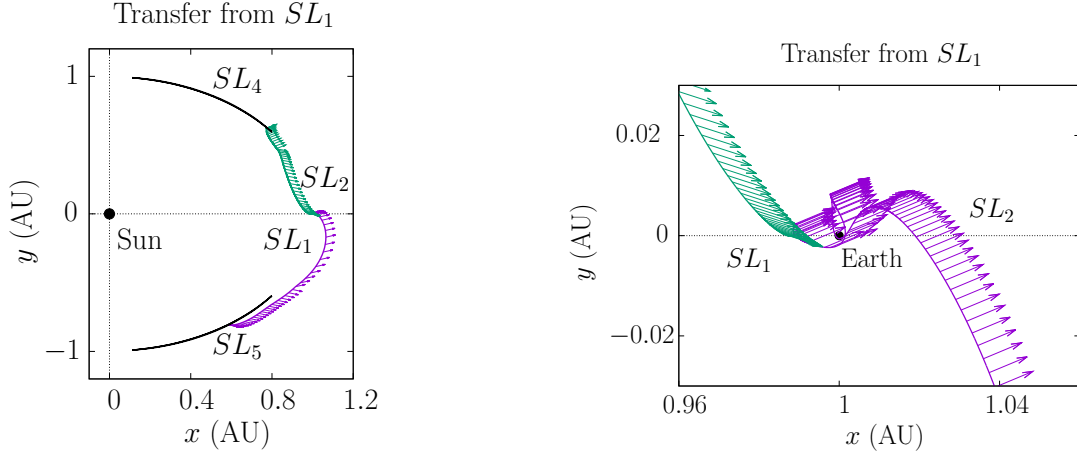


Figure 10. Selected transfer trajectories from SL_1 unstable manifold to the practical stability region around SL_4 (green) and SL_5 (purple). Left: full trajectories, Right: zoom close to the Earth.

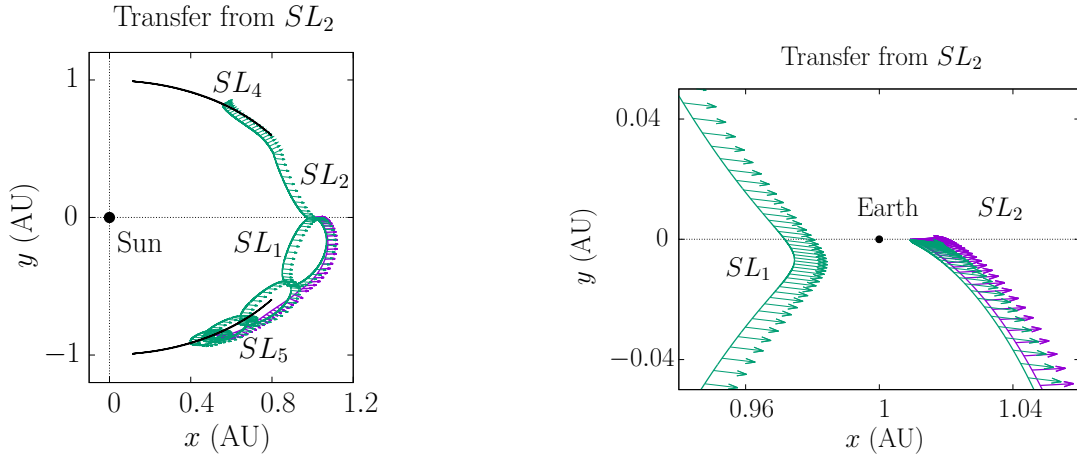


Figure 11. Selected transfer trajectories from SL_2 unstable manifold to the practical stability region around SL_4 (green) and SL_5 (purple). Left: full trajectories, Right: zoom close to the Earth.

addition, the small discontinuity in the state vector at the Poincaré section renders the trajectories unfeasible in practice. However, these solutions do provide an excellent initial guess to find time-optimal transfers between the SL_1/SL_2 points and the SL_4/SL_5 stability regions. For this, the accompanying optimal control problem needs to be defined and solved. In this paper, the latter is accomplished by using PSOPT,¹² which is a particular implementation of a direct pseudospectral method in C⁺⁺.

The goal is to find the time history of the states of the sailcraft, $\mathbf{x}(t) = [x, y, \dot{x}, \dot{y}]^T$, and its control, $u(t) = \alpha$, that minimize the transfer time from SL_1 and SL_2 to the stability regions around the triangular points. The objective can therefore be defined as:

$$J = t_f - t_0 \quad (13)$$

with t_f and t_0 the final and initial time of the trajectory. The dynamics that need to be satisfied are those in Eq. 1, though reduced to two-dimensional form, restricting the motion to the ecliptic plane. The start of the transfer needs to coincide with the displaced L_1 or L_2 points whose state vectors are given by $\mathbf{x}_{dL} = [x_{dL}, 0, 0, 0]^T$ with values for x_{dL} given in Table 2 for a range of solar sail lightness numbers. The boundary condition on the initial state vector can then be defined as:

$$\mathbf{x}(t_0) = \mathbf{x}_{dL} \quad (14)$$

Furthermore, the end point of the trajectory needs to coincide with the \mathcal{R} at SL_4 or SL_5 and the sailcraft needs to arrive at that point with zero synodical velocity. To allow the optimizer to select the best arrival location within \mathcal{R} , two static parameters are defined, $\mathbf{p} = [r, \theta]^T$, where r and θ represent the polar coordinates of the arrival location around the triangular Lagrange point as per the analysis in Section III.B. In order for these polar coordinates to lie within the stability region, the following constraints are applied. First (and equal to Eq. 12):

$$\left(\frac{r}{r_{max}}\right)^2 + \left(\frac{\theta}{\theta_{max}}\right)^2 \leq 1 \quad (15)$$

with $r_{max} = 0.0002$ and $\theta_{max} = 0.065$. Then, to ensure that the final state vector matches this arrival location, the polar coordinates r and θ are transformed into Cartesian position coordinates, (x_R, y_R) as per Eq. 11. This then enables the definition of the following additional constraint on the final state vector:

$$\mathbf{x}(t_f) = [x_R, y_R, 0, 0]^T \quad (16)$$

Eqs. 14 to 16 form the set of event constraints.

Finally, the bounds on the states, control and parameters need to be defined where the bounds on the states are case-specific. For example, for the transfer from SL_1 to SL_5 they are defined as:

$$[0, -1, -0.25, -0.25]^T \leq \mathbf{x}(t) \leq [1.2, 0.1, 0.25, 0.25]^T \quad (17)$$

The bounds on the control, i.e., on the pitch angle are defined as above Eq. 3:

$$-\pi/2 \leq u(t) \leq \pi/2 \quad (18)$$

Note that, other than the bounds defined above, no limitations on the steering capabilities are introduced, but will be considered in future work. Finally, the bounds on the parameters are set as:

$$[-r_{max}, -\theta_{max}]^T \leq \mathbf{p} \leq [r_{max}, \theta_{max}]^T \quad (19)$$

To solve the optimal control problem defined above, the minimum-time trajectories from Section IV.A are used as an initial guess. Results have been obtained for four different sets of transfers: from SL_1 to the region \mathcal{R} at SL_4 and SL_5 similarly from SL_2 . The first result, for a transfer from SL_1 to SL_4 and $\beta = 0.01$, appears in Figure 12 with numerical values in Table 5. The transfer itself is shown in the top-left image with a zoomed view of the initial and final conditions in the top-right image. These figures show that the optimizer converges to a solution that targets the outer edge of the stability region closest to Earth where $\mathbf{p} = [0, 0.065]^T$. This shortens the distance to be traveled and therefore minimizes the time of flight to 669 days, reducing the time of flight compared to the solution in Section IV.A by 12 days or 1.7%, see Table 5. Details on the control are provided in the bottom two images of Figure 12 which show the solar sail normal vector and solar sail pitch angle, respectively. Both show a relatively smooth control profile, though requiring rapid switches to orientations where the sail is “switched off”, i.e., when $\alpha = 90$ deg. As mentioned, future investigations will explore options to constrain the solar sail steering capabilities, e.g., similar to the work by Heiligers et al²⁵ though such limitations will come at the cost of an increase in the time of flight.

Table 5. Initial guess and optimized transfer times

	Initial guess $\beta = 0.01$	Optimized $\beta = 0.01$	Gain w.r.t. initial guess	Optimized $\beta = 0.02$	Optimized $\beta = 0.03$	Optimized $\beta = 0.04$	Optimized $\beta = 0.05$
$SL_1 - SL_4$	681	669	1.7%	458	386	336	320
$SL_1 - SL_5$	1298	986	24.1%	703	602	563	538
$SL_2 - SL_4$	3568	1430	59.9%	843	630	532	469
$SL_2 - SL_5$	988	888	10.1%	645	564	522	494

Using the result from Figure 12 as an initial guess, a continuation on the value for β can be initiated to obtain results for lightness numbers larger than $\beta = 0.01$. Note that a change in β requires a change in the location of the displaced Lagrange points and therefore a change in the boundary conditions in Eq. 14 and Eq. 16. The results for the transfer from SL_1 to SL_4 are shown in the top row of Figure 13 and the first row of Table 5. Especially the zoomed image on the right hand-side shows the shift in both SL_1 and the

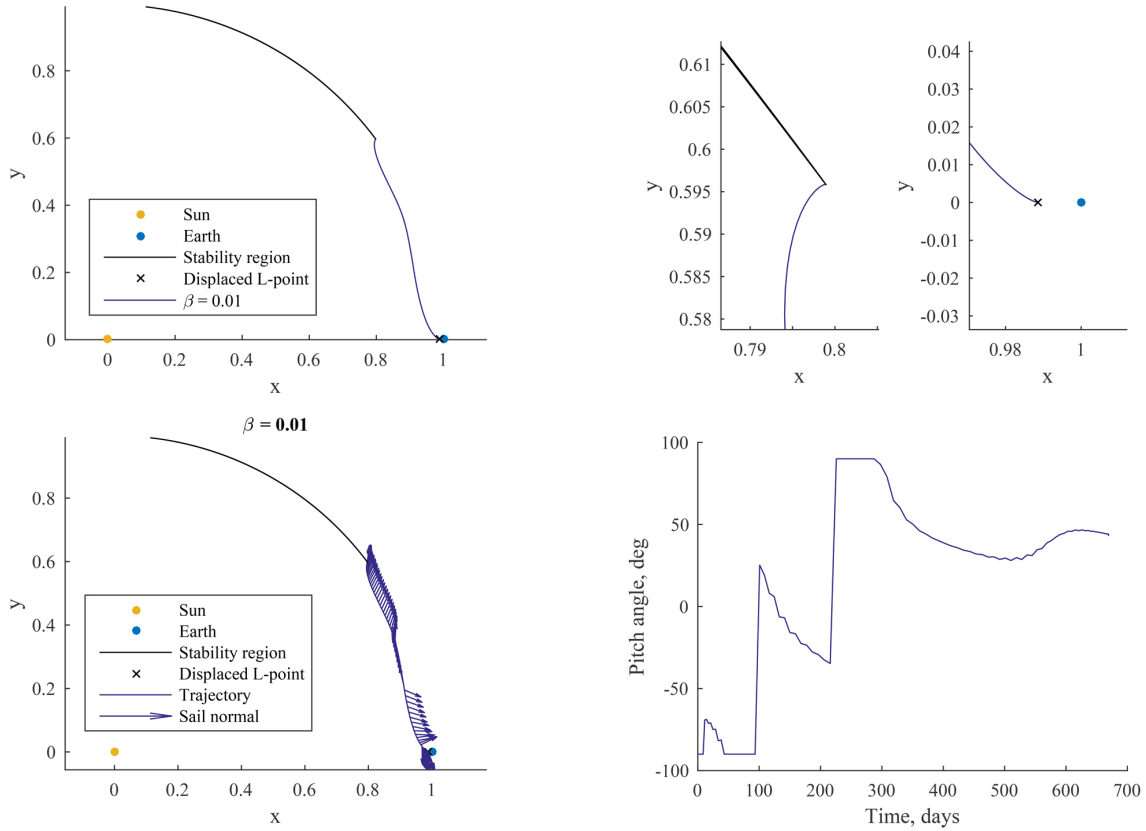


Figure 12. Top left: Time-optimal transfer from SL_1 to SL_4 stability region. Top right: Details of initial and final conditions. Bottom-left: Transfer including solar sail normal vector. Bottom-right: Control profile.

stability region around SL_4 with the value of β . The trend in the time of flight as a function of β appears in Figure 14 as a solid blue line and shows that by increasing the lightness number to a value of $\beta = 0.05$, the transfer time can be reduced to 320 days, which is less than half the transfer time for $\beta = 0.01$ (see also Table 5).

Conducting similar analyses for the transfers from SL_1 to SL_5 and from SL_2 to SL_4/SL_5 gives the transfers in the bottom row of Figure 13 and Figure 15 with corresponding times of flight in Table 5 and Figure 14. Comparing the transfer from SL_1 to SL_4 with the one from L_1 to L_5 shows a significantly longer time of flight for the latter as the optimizer only finds feasible trajectories that pass by the L_2 point. A similar comparison and conclusion can be drawn for the transfer from SL_2 to SL_4 that can only be achieved by passing by the L_1 point. However, still a significant reduction in time of flight can be realized compared to the initial guess: 24.1% and 59.9% for the SL_1 to SL_5 and SL_2 to SL_4 transfers, respectively. The improvement for the SL_1 to SL_5 transfer is mainly due to the fact that the optimizer targets the edge of the stability region, while the initial guess enters the stability region much closer to the SL_5 . Furthermore, the improvement of 59.9% for the SL_2 to SL_4 transfer is due to the fact that the optimized transfer no longer has to pass by the L_5 point (see Figure 11 left) and can instead directly connect the SL_2 and SL_4 points. Finally, the results for varying values for the lightness number in Figure 14 show similar reductions in times of flight between $\beta = 0.01$ and $\beta = 0.05$ as for the transfer from L_1 to L_4 : between 44.4% and 67.2%.

A final analysis carried out for the time-optimal transfers from SL_1/SL_2 to SL_4/SL_5 considers the effect of the size of the stability region around the triangular Lagrange points. This size can be varied by changing the bounds on the parameter θ , see Eq. 19. Results are created in a continuation where now the lightness number is fixed and the value of θ_{max} is slowly reduced. The results for $\beta = 0.01$ and $\theta_{max} = [0.065, 0.06, 0.055, \dots, 0.005]$ appear in Figure 16 for the transfer from SL_1 to SL_4 . Note that, the smaller the value for θ_{max} , the smaller the stability region. The stability region for the smallest value for θ_{max} ($\theta_{max} = 0.005$) is shown in the top-right plot of Figure 16. Through the continuation, the optimizer

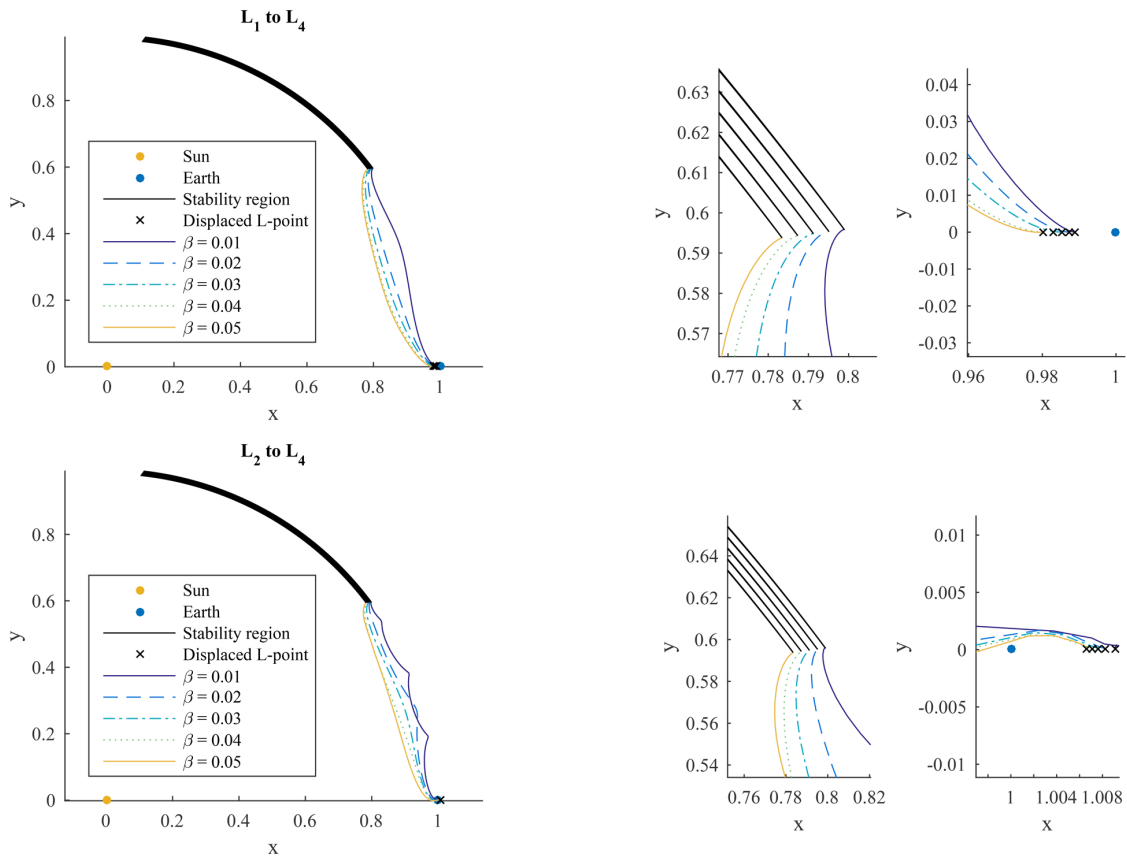


Figure 13. Time-optimal transfers from SL_1/SL_2 to SL_4 stability region. Figures on the right are close-ups of the trajectories on the left. Top row: SL_1 to SL_4 transfer. Bottom row: SL_2 to SL_4 transfer.

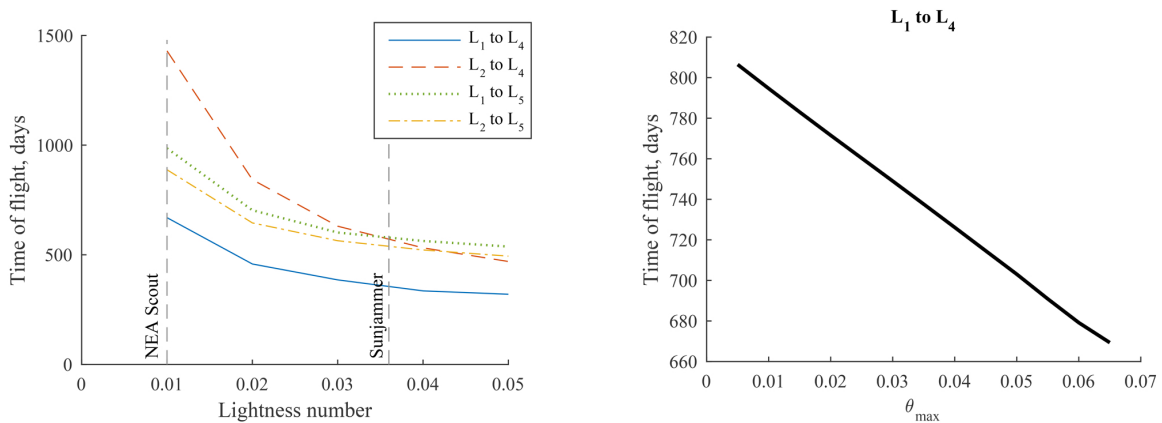


Figure 14. Optimal times of flight for transfers from SL_1/SL_2 to stability regions at SL_4/SL_5 . Left: as a function of the solar sail lightness. Right: as a function of θ_{max} .

can easily adapt to the change in stability region size and always converges to a solution where the transfer enters the stability region at the point closest to Earth, which is clearly demonstrated in the top-right plot of Figure 16. The effect on the time of flight appears in the bottom figure in Figure 16, which shows an approximately linear relation between the time of flight and θ_{max} . For $\theta_{max} = 0.005$ the transfer time is increased to 806 days compared to 669 days for the nominal value of $\theta_{max} = 0.065$.

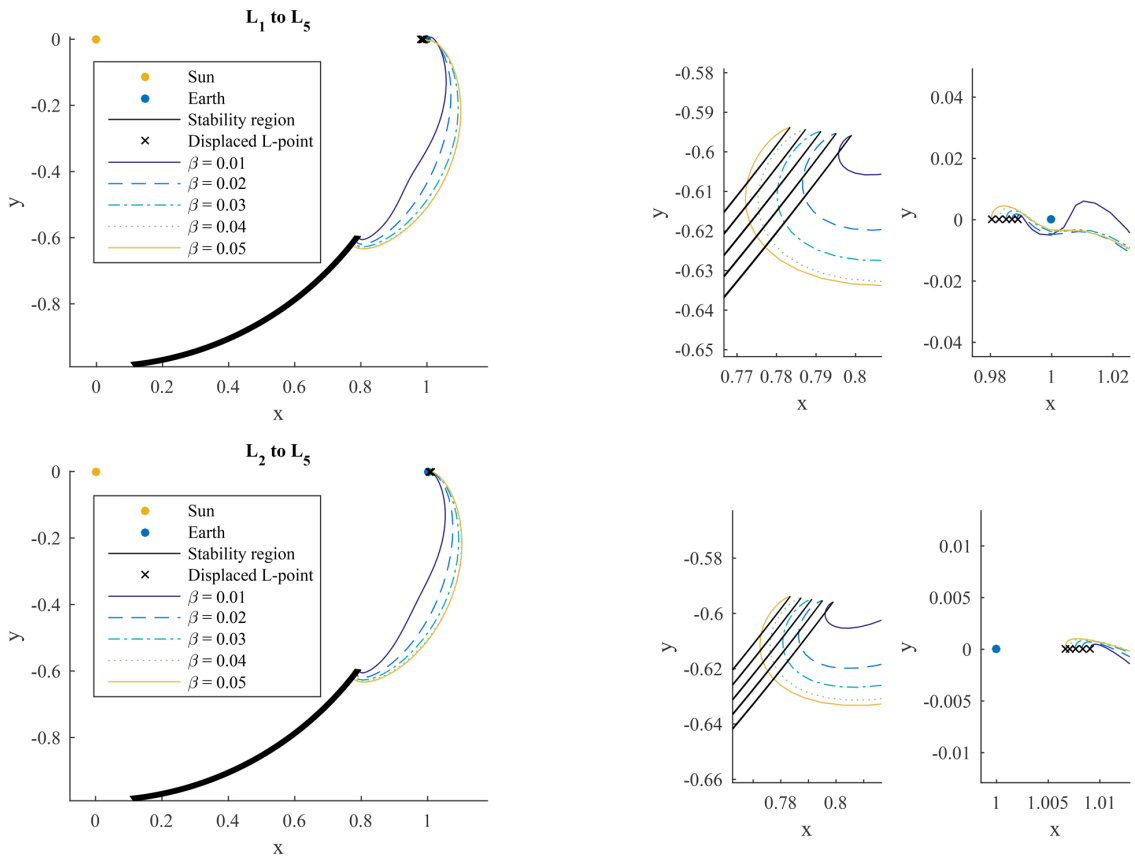


Figure 15. Time-optimal transfers from SL_1/SL_2 to SL_5 stability region. Figures on the right are close-ups of the trajectories on the left. Top row: SL_1 to SL_5 transfer. Bottom row: SL_2 to SL_5 transfer.

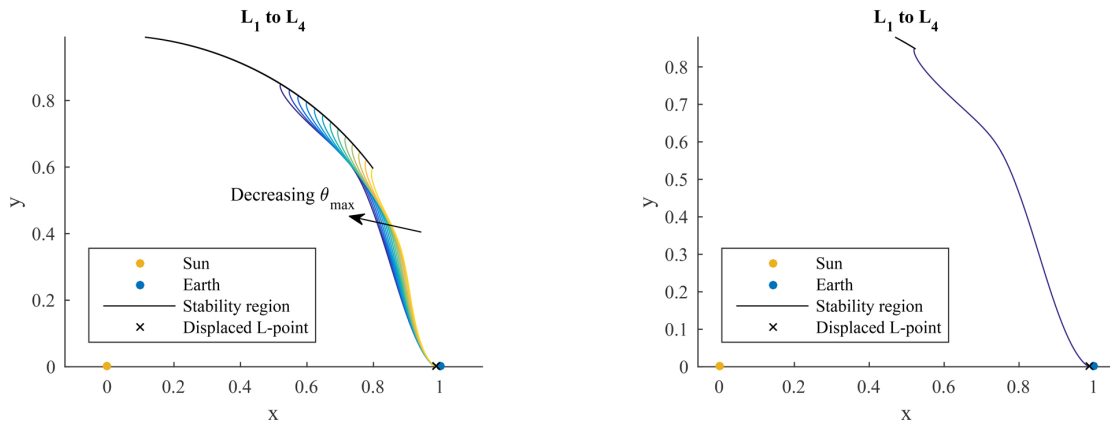


Figure 16. Time-optimal transfers from SL_1 to SL_4 stability region with $\beta = 0.01$ for different values for θ_{max} . Right: Transfers for $\theta_{max} = [0.065, 0.06, 0.055, \dots 0.005]$. Left: Transfer for $\theta_{max} = 0.005$.

V. Conclusions

In this paper we have analyzed the feasibility of using solar sails to find transfer trajectories from the L_1/L_2 equilibrium points to the regions of practical stability (RPS) that appear in the vicinity of L_4/L_5 . We have performed a preliminary analysis to study the dynamical implications on these regions due to changes in the solar sail parameters and we have used this information to find simple trajectories that transfer from

one region to the other. We have found time-optimal transfers by means of a pseudospectral optimization method using these simple trajectories as initial guesses.

Looking at the dynamics around L_1/L_2 , we have seen that when the sail is perpendicular to the Sun-sail line, both equilibrium points, and all the invariant objects around them, are shifted towards the Sun. The local stable and unstable manifolds display a similar qualitative behavior, but as we leave their vicinity, we see a significant change in their behavior. For instance, in the classical RTBP (no solar sail) a branch of the L_1 unstable manifolds extends towards the L_4 neighborhood, while the other branch gets trapped in the Earth's vicinity. This impedes to define transfer trajectories to L_5 using the invariant manifold of L_1 . But it is remarkable that as the sail lightness number increases we see that the branch that was trapped close to the Earth for $\beta = 0$ now manages to escape, providing transfers towards the L_5 neighborhood. Moreover, as we change the sail orientation, the manifold behavior becomes richer and we can take advantage of it.

Concerning the dynamics around L_4/L_5 , since these are totally elliptic equilibria for the RTBP, there is a region of practical stability around them. That is, orbits starting close enough to L_4/L_5 with zero synodical velocity remain close to these equilibria for extremely long times. Hence, no station keeping strategies are required. We have shown that this behavior is preserved once the effect of solar radiation pressure is added. We have studied the variation of the size of this region as β varies, and also which how orbits, that start there, propagate. We concluded that it makes sense to define a target region that could be written in closed form depending on the sail lightness number.

Combining the non-linear dynamics around L_1/L_2 and L_4/L_5 for $\beta \neq 0$ and $\alpha \neq 0$ we can find different two-maneuver transfer trajectories that go from one region to the other. The idea is to match a trajectory leaving the displaced SL_1 and SL_2 equilibria along the unstable manifolds with a fixed sail orientation α_0 with a trajectory reaching the RPS at the displaced SL_4/SL_5 with a fixed sail orientation α_1 . The change from one orientation to the other is performed at the mid-distance between the two points (a Poincaré section $\Sigma_1 = \{y = \pm(x + \mu)/\sqrt{3}\}$).

Using this simple approach we have been able to find, for $\beta = 0.01$, transfer trajectories joining all of the different regions: (a) from SL_1 to RPS at SL_4 , (b) from SL_1 to RPS at SL_5 , (c) from SL_2 to RPS at SL_4 and (d) from L_2 to RPS at L_5 . From all the trajectories that we have explored, we have seen that there is a larger variety of transfer options starting at SL_1 towards both SL_4/SL_5 RPS, than from SL_2 . Moreover, in general the transfer times from SL_1 are smaller than from SL_2 , although these trajectories are not time-optimal as a simple shooting method has been used to find them. One could easily decrease the transfer time by allowing a continuous change on the sail orientation.

Finally, using these manifold-type trajectories as an initial guess in a direct pseudospectral optimization method, time-optimal transfers between the displaced SL_1 and SL_2 points and the RPS at SL_4 and SL_5 are found. All transfers converge to a solution where the sailcraft enters the RPS at the point closest to Earth as this constitutes the shortest path. As such, improvements in the time of flight of 1.7% to 59.9% can be achieved with respect to the initial guess, depending on which of the four transfers is considered. The largest improvement of 59.9% is achieved for the transfer from SL_2 to SL_4 for which manifold-type trajectories can only be found by passing by the SL_5 point, while the time-optimal solution shows a direct transfer between SL_2 and SL_4 . Finally, increasing the lightness number from a near-term value of $\beta = 0.01$ to a maximum, far-term value of $\beta = 0.05$ allows further reductions in the time of flight of 44.4% to 67.2%.

VI. Future work

In this paper we have restricted ourselves to the dynamics of the RTBPS in the ecliptic plane $z = 0$. Since the full RPS is a 3D set, potential future directions of this research project is to study transfers towards L_4/L_5 where the target region contains points with $z \neq 0$.

One expects to be able to proceed analogously, by a first exploration using the two-step strategy exposed in Section IV.A, but using other invariant objects as gateways to a suitable 3D vicinity of SL_4/SL_5 . We know the natural dynamics around the two collinear equilibrium points is very rich, where we find different families of periodic and quasi-periodic orbits. It seems reasonable to consider the unstable invariant manifolds related to these periodic orbits as gateways towards the 3D RPS. In particular, due to their relevance in current mission applications, we will focus on the halo-type periodic orbits around the displaced L_1 and L_2 points.

Concerning the vicinity of the displaced SL_4/SL_5 equilibrium points, a suitable strategy to approximate the full 3D RPS is by using the method in Section III.B1 for $z = \text{constant}$ slices. As an example, we computed an approximation of the full 3D RPS for $\beta = 0.01$, which can be seen in Figure 17. To approximate this set,

we had to consider $T_{\max} = 10^4$ or even $T_{\max} = 10^5$, so for smaller values of T , say for reasonable mission time spans, the RPS would be much larger. Note that the full RPS has points whose z component is $\mathcal{O}(1)$, but it is still much narrower in r than in θ .

Preliminary computations for values of $\beta \in [0, 0.05]$ show that also in the 3D problem one can define a vicinity of the SL_4/SL_5 points in the (r, θ, z) variables that serves as common target region.

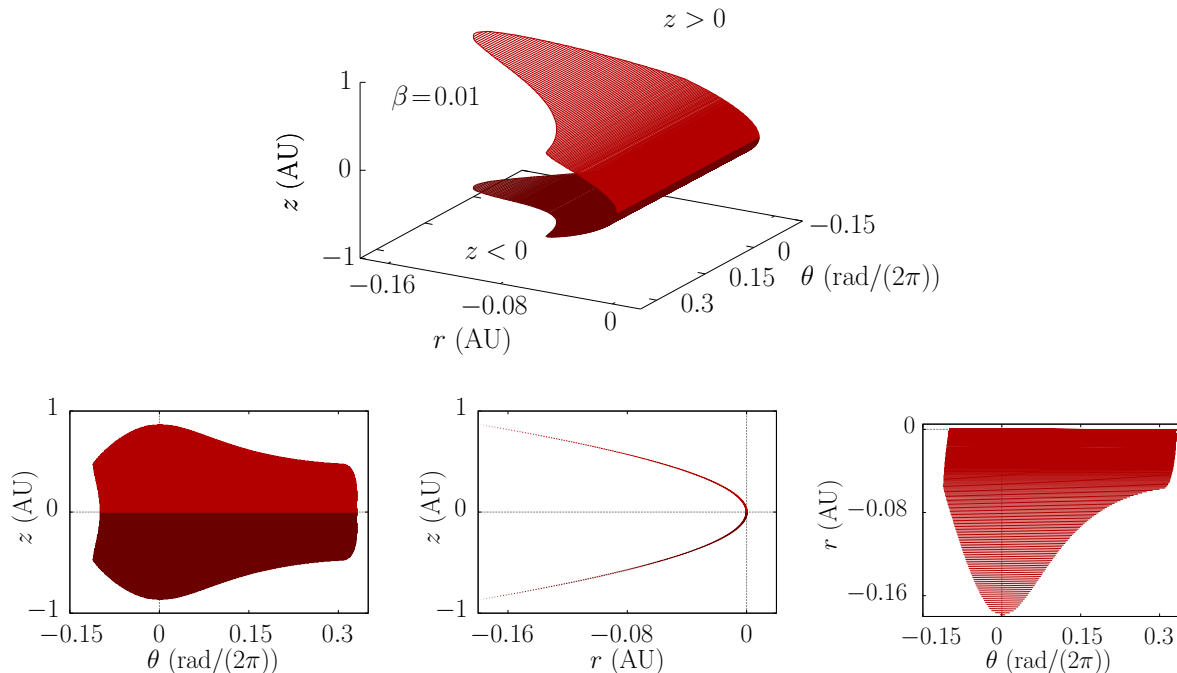


Figure 17. Complete region of practical stability around L_4 for $\beta = 0.01$. **Top:** 3D view. **Bottom left:** front view ($\theta - z$). **Bottom middle:** side view ($r - z$). **Bottom right:** raised view ($\theta - r$).

Acknowledgments

The research by AF has been supported by the Spanish grant MTM2015-67724-P (MINECO/FEDER) and the Catalan grant 2014 SGR 1145. The research by NM has been supported by the Spanish grant MTM2016-80117-P (MINECO/FEDER) and the Catalan grant 2014 SGR 1145.

JH acknowledges the support of the Marie Skłodowska-Curie Individual Fellowship 658645 - S4ILS: Solar Sailing for Space Situational Awareness in the Lunar System.

The authors would also like to thank J. Timoneda for the maintenance task of the computing facilities of the Dynamical System Group and the Facultat de Matemàtiques i Informàtica of the Universitat de Barcelona, that have largely been used in this work.

References

- ¹“Sunjammer: Preliminary End-to-End Mission Design,” August 2014.
- ²Forward, R. L., “Statite: A Spacecraft That Does Not Orbit,” *Journal of Spacecraft*, Vol. 28, No. 5, 1990, pp. 606–611.
- ³Macdonald, M., Hughes, G., McInnes, C., Lyngvi, A., Falkner, P., and Atzei, A., “GeoSail: An Elegant Solar Sail Demonstration Mission,” *Journal of Spacecraft and Rockets*, Vol. 44, 2007, pp. 784–796.
- ⁴Peloni, A., Ceriotti, M., and Dachwald, B., “Solar-Sail Trajectory Design for a Multiple Near-Earth-Asteroid Rendezvous Mission,” *Journal of Guidance, Control, and Dynamics*, Vol. 39, 2016, pp. 2712–2724.
- ⁵McInnes, C., *Solar Sailing: Technology, Dynamics and Mission Applications*, Springer-Praxis, 1999.
- ⁶Sood, R. and Howell, K., “ L_4, L_5 Solar Sail Transfers and Trajectory Design: Solar Observations and Potential Earth Trojan Exploration,” *26th AAS/AIAA Space Flight Mechanics Meeting*, February 2016.

- ⁷Farrés, A., “Transfer orbits to L_4 with a solar sail in the Earth-Sun system,” *Acta Astronautica*, Vol. 137, August 2017, pp. 78–90.
- ⁸Koon, W., Lo, M., Marsden, J., and Ross, S., *Dynamical Systems, the Three-Body Problem and Space Mission Design*, Marsden Books, 2011.
- ⁹Simó, C., “Boundaries of Stability,” Slides.
- ¹⁰Simó, C., Sousa-Silva, P., and Terra, M., “Practical stability domains near $L_{4,5}$ in the restricted three-body problem: some preliminary facts,” *Progress and challenges in dynamical systems*, Vol. 54 of *Springer Proc. Math. Stat.*, Springer, Heidelberg, 2013, pp. 367–382.
- ¹¹Llanos, P., Miller, J., and Hintz, G., “Mission and Navigation Desing of Integrated Trajectories to L_4/L_5 in the Sun-Earth System,” *Aerospace Research Central & American Institute of Aeronautics and Astronautics, Inc.*, Septiembre 2012.
- ¹²Becerra, V. M., “Solving Complex Optimal Control Problems at No Cost with PSOPT,” Sept 2010, pp. 1391–1396.
- ¹³Szebehely, V., *Theory of orbits. The restricted problem of three bodies*, Academic Press, 1967.
- ¹⁴Dachwald, B., Seboldt, W., Macdonald, M., Mengali, G., Quarta, A., McInnes, C., Rios-Reyes, L., Scheeres, D., Wie, B., Görlich, M., et al., “Potential Solar Sail Degradation Effects on Trajectory and Attitude Control,” *AAS/AIAA Astrodynamics Specialists Conference*, 2005.
- ¹⁵McInnes, A., *Strategies for Solar Sail Mission Design in the Circular Restricted Three-Body Problem*, Master’s thesis, Purdue University, August 2000.
- ¹⁶Farrés, A. and Jorba, À., “Periodic and Quasi-Periodic motions of a Solar Sail around the family SL_1 on the Sun-Earth System,” *Celestial Mechanics and Dynamical Astronomy*, Vol. 107, 2010, pp. 233–253.
- ¹⁷Sevryuki, M., *Reversible Systems*, Springer-Verlag, Berlin, 1986.
- ¹⁸Lamb, J. and Roberts, J., “Time-reversal symmetry in dynamical systems: a survey,” *Phys. D*, Vol. 112, 1998, pp. 1–39.
- ¹⁹Farrés, A. and Jorba, À., “On the High Order Approximation of the Centre Manifold for ODEs,” *Discrete and Continuous Dynamical Systems - Series B (DCDS-B)*, Vol. 14, October 2010, pp. 977–1000.
- ²⁰McInnes, C., McDonald, A., Simmons, J., and MacDonald, E., “Solar Sail Parking in Restricted Three-Body System,” *Journal of Guidance, Control and Dynamics*, Vol. 17, No. 2, 1994, pp. 399–406.
- ²¹Farrés, A., *Contribution to the Dynamics of a Solar Sail in the Earth-Sun System*, Ph.D. thesis, Universitat de Barcelona, 2009.
- ²²Farrés, A. and Jorba, À., “Artificial Equilibria in the RTBP for a Solar Sail and Applications,” *Proceedings of the Astronet-II International Final Conference*, Tossa de Mar, Catalunya, June 2015.
- ²³Farrés, A. and Miguel, N., “Solar Sailing at the L_4/L_5 Libration points,” *AAS/AIAA Astrodynamics Specialist Conference*, August 2017.
- ²⁴Gómez, G., Jorba, À., Masdemont, J., and Simó, C., *Dynamics and Mission Design Near Libration Points - Volume IV: Advanced Methods for Triangular Points.*, Vol. 5 of *World Scientific Monograph Series in Mathematics*, World Scientific, 2001.
- ²⁵J., H., G., M., and C.R., M., “Optimal solar sail transfers between Halo orbits of different Sun-planet systems,” *Advances in Space Research*, Vol. 55, 2015, pp. 1405–1421.